JACS
JOURNAL OF THE AMERICAN CHEMICAL SOCIETY

Article

pubs.acs.org/JACS

Dynamics of a Room Temperature Ionic Liquid in Supported Ionic Liquid Membranes vs the Bulk Liquid: 2D IR and Polarized IR Pump–Probe Experiments

Jae Yoon Shin, Steven A. Yamada, and Michael D. Fayer*

Department of Chemistry, Stanford University, Stanford, California 94305, United States

ABSTRACT: Supported ionic liquid membranes (SILMs) are membranes that have ionic liquids impregnated in their pores. SILMs have been proposed for advanced carbon capture materials. Two-dimensional infrared (2D IR) and polarization selective IR pump–probe (PSPP) techniques were used to investigate the dynamics of reorientation and spectral diffusion of the linear triatomic anion, $SeCN^-$, in poly(ether sulfone) (PES) membranes and room-temperature ionic liquid (RTIL), 1-ethyl-3-methylimidazolium bis(trifluoromethylsulfonyl)-imide (EmimNTf$_2$). The dynamics in the bulk EmimNTf$_2$ were compared to its dynamics in the SILM samples. Two PES membranes, PES200 and PES30, have pores with average sizes, ~300 nm and ~100 nm, respectively. Despite the relatively large pore sizes, the measurements reveal that the reorientation of $SeCN^-$ and the RTIL structural fluctuations are substantially slower in the SILMs than in the bulk liquid. The complete orientational randomization, slows from 136 ps in the bulk to 513 ps in the PES30. 2D IR measurements yield three time scales for structural spectral diffusion (SSD), that is, the time evolution of the liquid structure. The slowest decay constant increases from 140 ps in the bulk to 504 ps in the PES200 and increases further to 1660 ps in the PES30. The results suggest that changes at the interface propagate out and influence the RTIL structural dynamics even more than a hundred nanometers from the polymer surface. The differences between the IL dynamics in the bulk and in the membranes suggest that studies of bulk RTIL properties may be poor guides to their use in SILMs in carbon capture applications.

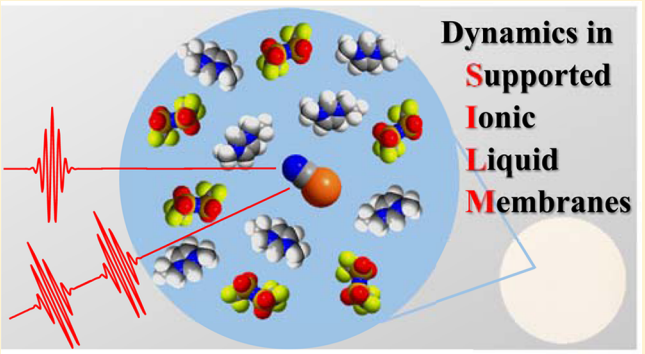

1. INTRODUCTION

The atmospheric concentration of the major anthropogenic greenhouse gas, CO_2, has tremendously increased since the industrial revolution, resulting in global warming and the onset of climate change. The globally averaged concentration of atmospheric CO_2 in 2015 was 399 ppm, which is far above the range of CO_2 concentrations over the past 800 000 years before industrialization (180–300 ppm).[1] Moreover, the growth rate of CO_2 is increasing, and the atmospheric CO_2 concentration will keep rising if the trend continues.[1]

To reduce the current CO_2 emission while sustainable energy system rollout progresses, the concept of carbon capture and storage (CCS) has been proposed.[2,3] Many aspects of CCS, such as technologies and economic costs for practical utilization, have been extensively investigated.[4−10] It is important to recognize that even after elimination of all fossil fuel power plants, 21% of stationary sources of CO_2 emission would remain from other industrial sources, e.g., chemical and cement production facilities.[11] Therefore, CCS will remain important after fossil fuel production of electricity has been reduced or eliminated.

In the CCS process, CO_2 is separated from other gases and captured before it enters the atmosphere at large stationary sources. The captured CO_2 is compressed and transported to oceanic or geological storage sites for permanent storage. Recent studies have discovered that injected CO_2 into underground layers of volcanic rock, basalt, resulted in 95% conversion of the CO_2 into carbonate minerals in less than 2 years, permanently locking up CO_2 underground without leakage.[12−14] Even though current technologies can capture up to 95% of CO_2,[2] the CO_2 separation is very energy intensive, dramatically increasing the monetary and environmental costs of the CCS process.[3] For example, the solvent absorption and physical adsorption techniques of the CO_2 separation utilize large temperature and pressure swings to strip off the absorbed or adsorbed CO_2 for transport and regeneration of the solvent or capturing material.[15,16] Another technique, cryogenic fractionation also requires high energy consumption for lowering the temperature to condense CO_2.[15,16] The capture/separation step is the most costly ($55 to $112/ton CO_2) process in CCS and inhibits its practical application.[12,17] Therefore, it is important to develop better methods and materials for the CO_2 separation.

Room-temperature ionic liquids (RTILs) have recently emerged and attracted much attention as a medium for the

Received: October 14, 2016
Published: December 14, 2016

DOI: 10.1021/jacs.6b10695
J. Am. Chem. Soc. 2017, 139, 311–323

CO_2 capture.[18−22] Ionic liquids (ILs) are defined as molten salts, usually consisting of a large asymmetric organic cation, anion, or both, that have melting points below 100 °C.[23] When ILs remain liquid at room temperature, they are called RTILs. In general, RTILs have negligible volatility,[24] low flammability,[25] and high thermal stability.[26] More important, their physical and chemical properties can be fine-tuned by combining various kinds of cations and anions.[23,27] Therefore, using RTILs as the CO_2 separation medium can be advantageous over using organic solvents such as amine-based solvents in traditional postcombustion CO_2 capture techniques where the degradations and loss of solvents are problematic.[5,15,28]

The emergence of RTILs as a CO_2 capture medium led to the idea of combining RTILs and membrane technologies, resulting in what are called supported ionic liquid membranes (SILMs).[29−32] The SILMs are based on porous solid materials (organic or inorganic membranes) that are impregnated with RTILs in their pores. The SILMs are cost- and energy-effective materials because they consume only small amounts of RTILs and do not need a CO_2 stripping step for solvent regeneration, which requires intense energy consumptions and high costs.[29−32] In addition, the low volatility and high viscosity of RTILs promise an enhanced stability of SILMs as compared to the conventional supported liquid membranes (SLMs) where common organic solvents are immobilized in the pores, enabling SILMs to last longer during operation.[29] The CO_2 separation with SILMs was reported in 2002 for the first time.[29] Since then, many types of SILMs prepared with a variety of supporting materials and RTILs have been developed and tested to optimize their performances for the application.[32]

In general, most SILMs research reports on gas permeability and permselectivity, which are macroscopic properties, as a merit of performance and compare these to other SILMs, focusing on how well the target gas, such as CO_2, can permeate through the membrane relative to other gases.[32] However, there has been no effort to understand the properties of SILMs on a molecular level. Very recently the dynamics of CO_2 in the bulk ILs was explored, providing the useful insights into the role of ILs in CO_2 solvation and carbon capture applications.[33−35] Similar studies on SILM systems can be useful because a fundamental understanding of their underlying molecular interactions and dynamics will inform the rational design of SILM technologies.

Here we report spectral diffusion and orientational dynamics using the vibrational probe $SeCN^-$ in SILMs, employing ultrafast infrared nonlinear spectroscopies, that is, two-dimensional infrared (2D IR) vibrational echo and IR polarization selective pump−probe (PSPP) techniques. Both the spectral diffusion and the probe orientational relaxation are determined mainly by the RTIL dynamics. The effects of confinement on the dynamics and structure of the RTIL in the SILMs are explicated by comparing the observables measured using the $SeCN^-$ vibrational probe in the SILMs vs in the bulk liquid. Changes in the observables are caused by changes in the RTIL arising from confinement in the membrane. $SeCN^-$ was used in these experiments rather than CO_2 for several reasons. First the $SeCN^-$ has a longer vibrational lifetime than CO_2, making it possible to examine the dynamics in a wider time window. To prevent water uptake, the membrane, RTIL, and vibrational probe must be assembled into the sample cell in a glovebox, which is more difficult to when the vibrational probe is a gas. Furthermore, the spectral diffusion dynamics are influenced by Stark effect coupling to the electric fields produced by the RTIL.[34,36,37] Because it has a permanent dipole moment, $SeCN^-$ couples to the electric fields through a first order Stark effect,[37−39] while CO_2, with no permanent dipole moment, couples through the second order Stark effect.[34,40] The data analysis is more straightforward when the coupling is first order.[34,37] In 2D IR and orientational relaxation experiments performed on $SeCN^-$ in the bulk ionic liquid, 1-ethyl-3-methylimidazolium bis(trifluoromethylsulfonyl)imide (abbreviated as $EmimNTf_2$), which is the IL investigate in the SILMs, it was found that the functional forms of the observed time dependences were the same as those observed with CO_2 as the vibrational probe, but the time constants for CO_2 were approximately a factor of 3 faster. In chain length studies with the cation having ethyl, butyl, octyl and decyl side chains, the trends in the dynamics with chain length were the same for $SeCN^-$ and CO_2. Therefore, $SeCN^-$ is useful to determine if confinement in the membranes influences the RTIIL dynamics and structure.

The SILMs were prepared in two poly(ether sulfone) (PES) membranes with 200 and 30 nm nominal pore sizes. The PES membranes are stable polymer supports that can be used for the SILM preparation without warping or swelling.[29] In general, membranes with 100 to 200 nm pore sizes are used because the pore size affects the stability of SILMs, with the smaller pore sizes enhancing stability due to increased capillary force.[29,31,32] In this study, we used two hydrophilic PES membranes, PES200 and PES30 as representative SILMs. The embedded RTIL mainly determines the separation performance of SILMs.[31] The $EmimNTf_2$ studied here is a good candidate for CO_2 separation because it has a high CO_2 solubility[41,42] and good thermal and electrochemical stability.[43,44]

For the comparison to the neat liquid, we revisited $SeCN^-$ in bulk $EmimNTf_2$ with improved experimental ability that enables longer time dynamics to be measured. The new measurements remove a degree of uncertainty in part of the previous results. In bulk $EmimNTf_2$, $SeCN^-$ shows a multiexponential anisotropy decay (orientational relaxation) measured with PSPP experiments. The wobbling-in-a-cone model[45−51] was used to interpret the results, which show that there are restricted orientational motions followed by complete orientational randomization. Orientational relaxation time constants and cone angles were obtained from the analysis.

The linear absorption spectrum of the CN stretch of $SeCN^-$ is inhomogeneously broadened. The RTIL has a vast range of solvent structures that produce different interactions with the vibrational probe, giving rise to an array of CN stretch frequencies and consequently, inhomogeneous broadening. As the liquid structure evolves, the vibrational frequency of the probe will change within the range of frequencies contained in the inhomogeneously broadened absorption line. At sufficiently long time, all liquid structures that give rise to the frequencies in the absorption spectrum will be sampled by the vibrational probe. The time evolution of the vibrational frequency, which is caused by changes in the liquid structure, is called structural spectral diffusion (SSD). The 2D IR vibrational echo experiments measure the spectral diffusion of the CN stretch of $SeCN^-$ on time scales of hundreds of femtoseconds to hundreds of picoseconds. In addition to SSD, orientational relaxation of the probe molecule causes reorientation induced spectral diffusion (RISD). RISD can be quantified from the PSPP anisotropy measurements and separated from the SSD using the method that has been developed and applied previously.[36,37]

DOI: 10.1021/jacs.6b10695
J. Am. Chem. Soc. 2017, 139, 311−323

The PES membranes used in this study have relatively large pores (200 and 30 nm according to manufacturer specifications) compared to the other confined systems with few nanometer dimensions where the nanoconfinement effects can have a tremendous impact on molecular dynamics.[50,52−60] The pores in both PES200 and PES30 membranes have broad size distributions, and the average size is substantially larger than the manufacturer's value, that is ∼300 nm and ∼100 nm for the PES200 and PES30 membranes, respectively. Despite the very large pore sizes, the $EmimNTf_2$ dynamics in the SILMs are substantially different from those of the bulk liquid. Depending on the particular aspect of the observables, the dynamics in the pores are ∼1.5 to ∼4 times slower in the pores than in the bulk liquid. Therefore, the results demonstrate that the characteristics of SILMs cannot be predicted from the ILs' bulk properties.

2. EXPERIMENTAL PROCEDURES

2.1. Sample Preparation. $EmimNTf_2$ was dried under vacuum (∼100 mTorr) at ∼65 °C after purchase from Iolitec. Its water content was under 10 ppm as determined by coulometric Karl Fischer titration (Mettler Toledo). To introduce $SeCN^-$ into the IL, EmimSeCN was used so that no additional cations were added. EmimSeCN was prepared from KSeCN and Emim iodide (Acros and Iolitec respectively), following the procedure of Wang et al.[61] Both KSeCN and Emim iodide were dried under the same conditions as the $EmimNTf_2$ before being used. EmimSeCN was added to $EmimNTf_2$ at a molar ratio of 1:200 ion pairs, EmimSeCN:$EmimNTf_2$.

For the SILM preparation, poly(ether sulfone) membranes, PES200 (Supor 200) and PES30 (PES00313100) were purchased from Pall and Sterlitech corporations, respectively. We fill the membrane pores with the $EmimNTf_2$/ EmimSeCN solution by soaking the membrane in the solution overnight, and then wipe the membrane with lens tissues to remove solution on the surface. Since the PES200 and PES30 membranes have high porosities (60−80%) and have a thickness of ∼150 μm, any remaining solution on the surface would make a negligible contribution to the signals. The SILM was sandwiched between two one-inch CaF_2 windows with a polytetrafluoroethylene (Teflon) ring space. The spacer has a thickness of 150 μm, which is comparable to the thickness of membranes (110−150 μm). To prevent the membrane from being in contact with the windows, i.e., make it free-standing, we cut another Teflon spacer (150 μm) that has a hole in the middle and insert it between the SILM and window on both sides. In addition to making the membrane free-standing, as it would be in a CO_2 capture application, preventing the membrane from contacting the windows eliminated changes in the data over long time periods when the membrane was in contact with the window.

For the bulk sample preparation, the $SeCN^-$ solution was sandwiched between CaF_2 windows with a Teflon ring spacer (150-μm thick). All of the samples were prepared and stored under N_2-purged conditions to avoid contamination with H_2O. Linear Fourier transform infrared (FT-IR) spectra of the samples were collected using a Thermo Scientific Nicolet 6700 FT-IR spectrometer before and after the ultrafast IR experiments to confirm that there were no changes in the samples over time.

Nitrogen adsorption−desorption isotherms of the PES30 membrane were measured to obtain its pore size distribution using a gas sorption analyzer, Quantachrome Autosorb iQ3 (Soft and Hybrid Material Facility at Stanford University). Before the measurements, 50 mg pieces of PES30 membrane were degassed under vacuum at 120 °C for 24 h. From the desorption part of the isotherm, the pore size distribution was calculated based on the Barrett−Joyner−Halenda (BJH) model.[62] The PES200 pore size distribution is reported in the literature.[63]

2.2. Time-Resolved Ultrafast Infrared Experiments. The details of the experimental setup have been reported[64] previously, and only a brief description is presented here. A Ti:sapphire regenerative amplifier pumps a home-built optical parametric amplifier (OPA), which is based on a beta barium borate crystal, at a 1 kHz repetition rate, producing signal and idler in the near-IR region. Both output beams from the OPA are mixed in a $AgGaS_2$ crystal for difference-frequency generation, creating mid-IR pulses centered at 2064 cm^{-1} with ∼6 μJ pulse energy. The mid-IR beam was split into two beams, a stronger pump pulse and weaker probe pulse. The pump pulse was passed through an acousto-optic mid-IR Fourier-domain pulse-shaper. In the PSPP experiments, the pulse shaper chopped and phase cycled the pump pulse to obtain transient absorption signals, while in the 2D IR experiments the pulse shaper generated two excitation pulses, 1 and 2, and controlled the delay time (τ) between them.

The major difficulty in performing the membrane experiments was scattered light. The membranes look like a piece of opaque white filter paper. The scattering problem was overcome using the pulse shaper. In addition to the pulse timing the pulse shaper controls the phase of the pulses. For the liquid IL samples, a 4-shot phase cycling scheme was used for the 2D IR experiments as well as for the PSPP. For the membranes, an 8-shot phase cycling and chopping scheme was utilized in the 2D IR measurements, especially for the SILMs samples with PES30 membranes where the scattered light was particularly bad. A mechanical delay stage in the probe pulse path controls the time delay between the pump and probe pulses in the PSPP experiments or the time delay (waiting time, T_w) between the second excitation pulse 2 and the third excitation pulse 3 (probe pulse) in the 2D IR experiments. The pump and probe pulses were focused into the sample with a small crossing angle for both experiments. The probe pulse was directed into a spectrometer after passing through the sample. The spectrometer disperses the probe pulse, which was then detected in the frequency-domain by a 32-pixel HgCdTe (MCT) IR array detector. The 2D IR signal is collinear with the third pulse (probe pulse), which also acts as the local oscillator used for heterodyne detection of the signal.

In the PSPP measurements, the probe polarization was horizontal (in the plane of the optical table) and the pump polarization was at 45° with respect to the probe pulse. After the sample, a polarizer mounted in a computer controlled rotation stage alternately resolved the probe pulse at +45° (parallel to the pump) and −45° (perpendicular to the pump) relative to the incident polarization (horizontal). Since the response of the spectrometer grating is polarization-dependent, we placed another horizontal polarizer in front of the spectrometer entrance slit to ensure that there is no biased detection of the polarizations. The collected probe signals parallel, $S_{\parallel}(t)$, and perpendicular, $S_{\perp}(t)$, to the pump were used to obtain the population relaxation $P(t)$ and the second Legendre polynomial orientational correlation function $C_2(t)$ using[65]

$$S_{\parallel}(t) = P(t)[1 + 0.8C_2(t)] \tag{1}$$

$$S_{\perp}(t) = P(t)[1 - 0.4C_2(t)] \tag{2}$$

From these, the population relaxation is given by

$$P(t) = \frac{1}{3}[S_{\parallel}(t) + 2S_{\perp}(t)] \tag{3}$$

The anisotropy, $r(t)$, is the transition dipole orientational correlation function (the second Legendre polynomial correlation function, $C_2(t) = \langle P_2(\hat{\mu}(t)\cdot\hat{\mu}(0))\rangle$),

$$r(t) = \frac{S_{\parallel}(t) - S_{\perp}(t)}{S_{\parallel}(t) + 2S_{\perp}(t)} = 0.4C_2(t) \tag{4}$$

In the 2D IR vibrational echo experiments, three excitation pulses 1, 2, and 3 impinge on the sample with controllable time delays, τ (delay between 1 and 2 pulses) and T_w (delay between 2 and 3 pulses). In effect, pulses 1 and 2 label the initial frequencies of all of the CN stretch vibrational oscillators. After the system evolves during T_w, pulse 3 generates the vibrational echo signal, reading out the final frequencies of the vibrational oscillators. To carry out the polarization selective measurements, we set the polarization of both excitation pulses 1 and 2 to 0° and 90° relative to the probe polarization (horizontal) in the $\langle XXXX\rangle$ and $\langle XXYY\rangle$ configurations, respectively, using

DOI: 10.1021/jacs.6b10695
J. Am. Chem. Soc. 2017, 139, 311−323

a polarizer and half-wave-plate. The resolving polarizer after the sample is fixed to horizontal and is not changed for both polarization configurations. For the SILM samples, we are only able to collect the 2D IR spectra with the perpendicular, $\langle XXYY \rangle$, configuration because we observe severe interferences from the scattered light in the parallel, $\langle XXXX \rangle$, configuration. The perpendicular polarization configuration with phase cycling scheme substantially reduces the interferences from scattered light and makes the 2D IR experiments possible for solid samples such as the SILMs. The 2D IR spectrum consists of the ω_m (vertical) and ω_τ (horizontal) axes and needs two Fourier transforms to be constructed. The first Fourier transform yields the ω_m axis experimentally by resolving the frequencies of echo/LO pulse via the spectrometer, that is, the time domain pulse is taken to the frequency domain. Scanning τ in the experiments produces an interferogram at each ω_m because the echo signal moves in phase relative to the fixed in time LO. The numerical Fourier transform of this interferogram for each ω_m gives the ω_τ axis of the 2D IR spectrum.

For each T_w, a 2D IR spectrum is collected by scanning τ, and the spectral diffusion is evaluated based on the 2D line shape analysis at each T_w. The T_w-dependent frequency−frequency correlation function (FFCF) contains the dynamical information on interest. The center line slope (CLS) method was employed to obtain the FFCF from the 2D IR spectra.[66,67] To calculate the CLS at a given T_w, 1D spectra were obtained by slicing the 2D spectrum parallel to the ω_m axis for a range of ω_τ. These spectra were fit with Gaussian peak shape functions to determine the peak frequency. A plot of these peak frequencies is the center line. The CLS is the slope of the center line. As the system evolves with increased T_w, the CLS changes, from a possible maximum value of 1 to 0 when spectral diffusion is complete. A plot of the CLS vs T_w is the normalized T_w-dependent portion of the FFCF. Given the CLS(T_w) and the linear absorption spectrum, the full FFCF including the homogeneous component can be determined.[66]

3. RESULTS AND DISCUSSION

3.1. Pore Size Distributions of PES Membranes. To study and understand the dynamics of ILs and molecules inside the SILMs, characterization of the membranes' pore sizes is necessary. As mentioned above, the two poly(ether sulfone) membranes, PES200 and PES30 are commercial from different companies. According to the specifications, the pore sizes of PES200 and PES30 are 200 and 30 nm, respectively, which were determined by the size of retained particles in the membranes or bubble point testing.[68] These numbers are only for the purpose of filtration, the intended application, and they do not necessarily represent the mean pore size of the membranes. Additionally, no information about the pore size distribution is provided by the manufacturer.

The pores and their size distribution in the PES200 membrane have been characterized previously using scanning electron microscopy (SEM) and gas permeability measurements.[63] Figure 1 displays a SEM image and the pore size distribution of PES200, as well as the pore size distribution of PES30. The pore size distribution of PES200 comes from Ramakrishnan et al.[63] In the original work, the relative flow distribution plot emphasized the contribution from the large pores as the fourth power of the pore diameter.[63] We replotted their data in Figure 1 taking the square root of relative flow, which was normalized to the maximum value, as a function of pore size to compensate. Our plot is now the relative volume distribution, assuming cylindrical pores. As shown in Figure 1, the pore size distribution of PES200 is broad with a range from 80 to 500 nm and a maximum near 360 nm. The previous work estimated the mean pore size of PES200 to be 280 nm,[63] which is larger than the 200 nm manufacturer specifications. The SEM image also shows a broad distribution of large pore sizes.

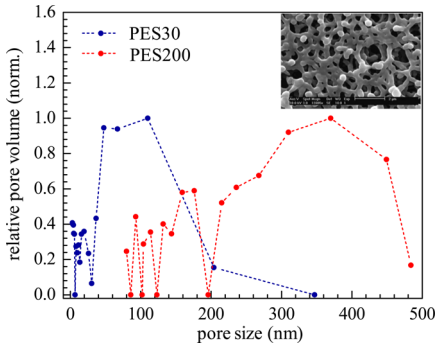

Figure 1. Pore size distributions of the PES200 and PES30 membranes. The data for PES200 was adopted from the gas permeability measurements study in ref 63 and modified to present normalized relative pore volume. The PES30 data is from N_2 adsorption/desorption isotherm measurements with the BJH method and is also normalized for the comparison. The inset shows the PES200 membrane's SEM image reprinted with permission from ref 63. Copyright 2004 Elsevier.

In contrast to PES200, the pore size distribution of the PES30 membrane has not been reported previously. We thus measured the N_2 adsorption/desorption isotherm of PES30 to obtain the pore size distribution using the BJH model.[62] The data displayed in Figure 1 reveals a broad distribution with a maximum near 110 nm. The pores in the PES30 have sizes between 40 and 200 nm, substantially larger than the 30 nm indicated by the manufacturer. This trend is consistent with that for PES200. The N_2 adsorption/desorption isotherm is measured at liquid nitrogen temperature, 77 K. At this temperature the membrane's volume may shrinks, possibly resulting in contraction of the pore size. Using the linear thermal expansion coefficient of poly(ether sulfone) (55×10^{-6} K^{-1}),[69] the volume shrinkage is calculated to be only 3.6% from room temperature to 77 K, which is a negligible amount of volume change given the width of the distribution. While the pore size distributions overlap, there is still a substantial difference in pore sizes, with those of PES200 significantly larger than those of PES30.

3.2. Linear IR Absorption Spectrum. Figure 2 shows the linear FT-IR absorption spectra of the CN stretch of $SeCN^-$ in

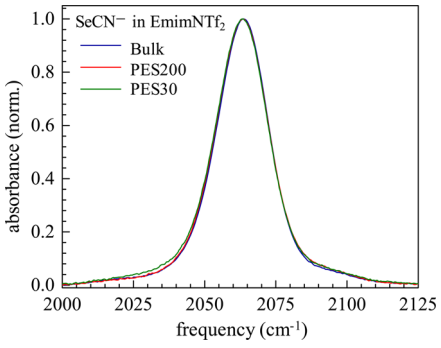

Figure 2. Background-subtracted and normalized FT-IR spectra of the CN stretching mode of $SeCN^-$ in the bulk $EmimNTf_2$ and the SILMs, PES200 and PES30.

$EmimNTf_2$ for the bulk and SILM (PES200 and PES30) samples. The neat, bulk $EmimNTf_2$ spectrum was subtracted from the spectrum of the bulk sample with $SeCN^-$, and the spectrum of the blank SILM (only containing $EmimNTf_2$ in the PES200 and PES30) was subtracted from that of the SILM sample

DOI: 10.1021/jacs.6b10695
J. Am. Chem. Soc. 2017, 139, 311−323

containing the $SeCN^-$ solution. The peak center is 2063.4 cm^{-1} with a full width at half-maximum (fwhm) of 21.3 cm^{-1} for the bulk when it is fit with a Voigt line shape. The spectra of the CN stretch in the SILM samples are essentially identical to the bulk sample spectrum within experimental error, as shown in Figure 2.

The center frequency of the CN stretch band of the $SeCN^-$ is sensitive to the surrounding solvent environment. In D_2O, the absorption band appears at 2075 cm^{-1}, blue-shifted due to hydrogen bonding interactions. In very small AOT reverse micelles (w_0 = 1), in which the $SeCN^-$ is interacting mainly with the SO_3^- head groups and Na^+ counterions, the band appears at 2065 cm^{-1}, which is close to the center frequencies in $EmimNTf_2$ and other ILs.[70] Here, the center frequency of the CN stretch does not change in the SILMs compared to that in the bulk RTIL. The pore sizes are so large in the SILMs that a negligible fraction of the $SeCN^-$ will be in close proximity to the pore walls. The $SeCN^-$ spectra suggest that the intermolecular interactions that determine the peak position and the fwhm are essentially unchanged in going from the bulk IL to the ILs confined in the pores.

Looking at the spectra alone, they suggest that confining the IL in the large pores minimally perturbs the range of liquid structures that give rise to the inhomogeneously broadened absorption line. The absorption spectrum of the OD hydroxyl stretch of dilute HOD in H_2O contained in AOT reverse micelles is essentially identical to the OD spectrum in bulk water when the diameter of the reverse micelles is greater than ~9 nm (w_0 = 25).[54,55] For smaller diameters, the OD spectrum develops a blue shoulder that arises from the non-negligible fraction of water molecules that are directly interacting with the AOT interface. Away from the interface, the water core of the reverse micelle is still bulk like. It is necessary to go to a diameter of ~4 nm before there is no bulk like water. Therefore, for the large pores of the SILMs and the very small fraction of the vibrational probe that is at the interface, one would initially assume that not only the spectrum, but all of the properties of the IL probed by $SeCN^-$ would be bulk like.

3.3. PSPP Measurements: Population and Reorientation Dynamics. The PSPP experiments measured the transient absorption signals with parallel and perpendicular polarization configurations, $S_{\parallel}(t)$ and $S_{\perp}(t)$, which were used to construct $P(t)$, the isotropic decay (population relaxation) and $r(t)$, the anisotropy, using eqs 3 and 4.

In general, the isotropic population decay, $P(t)$, in addition to the vibrational lifetime, can have contributions from spectral diffusion. For example, non-Condon effects can cause one side of a vibrational line to absorb more than the other.[38,70] The initial excited state population flows from one side of the line to the other via spectral diffusion.[51,70,71] At a particular wavelength within the absorption spectrum, the spectral diffusion can appear in $P(t)$ as nonexponential behavior on short time scales. Here, there are sharp solvent/polymer absorption bands under the $SeCN^-$ absorption spectrum although these bands do not appear in the absorption spectrum of Figure 2 after background subtraction. They also do not directly contribute to the nonlinear signal due to their small transition dipoles but influence the absorption because the species that give rise to them are in high concentration. Thus, they can absorb some of the pump pulse at certain frequencies, which causes somewhat nonuniform pumping of the $SeCN^-$ band, which affects $P(t)$. Population equilibration through spectral diffusion introduces the nonexponential decay of $P(t)$ at early times as in the case of non-Condon effects.

Therefore, to extract the vibrational lifetime of the CN stretch of $SeCN^-$, $P(t)$ was fit to a single-exponential using later time data from 100 to 400 ps. The fit yields lifetimes of 105 ± 1 ps for all the samples without showing distinct frequency dependence across the band near the center frequency. Vibrational lifetimes are generally very sensitive to the local environment of the vibrational oscillator. To vibrationally relax, the energy from the initially excited mode flows into a combination of intramolecular and intermolecular modes.[72,73] The intermolecular modes usually involve the continuum of low frequency modes of the bath, which are required for energy conservation. The vibrational lifetime depends on the density of states and the coupling to the bath modes. We found that the lifetime in the bulk liquid is the same as in the two SILMs. This result implies that the local environment of the $SeCN^-$ is not changed significantly in going from the bulk to the RTIL in the membrane pores. The unchanged vibrational lifetime in the SILMs is also evidence that $SeCN^-$ directly interacting with the pore walls does not significantly contribute to the nonlinear IR signals, and that there is no significant contribution to the experiments in the very small pores either.

In contrast to the absorption spectra and lifetimes, the anisotropy decays change in the SILMs samples as shown in Figure 3. Both SILM samples displayed slower reorientation

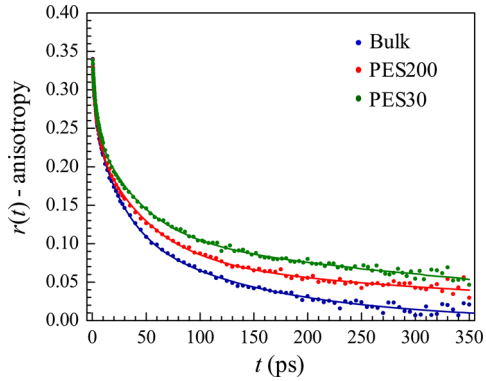

Figure 3. Anisotropy decays of $SeCN^-$ in bulk $EmimNTf_2$ and the same solution in the SILMs, PES200 and PES30 (points), with triexponential fits to the data (solid curves).

dynamics compared to the bulk sample. The anisotropy data for all the samples are frequency independent; each decay curve in Figure 3 is the average of eight curves from detection frequencies between 2061 and 2070 cm^{-1}. The anisotropy decays from the three samples were fit with triexponential functions, and the resulting fit parameters are given in Table 1. In a previous study of $EmimNTf_2$ using EmimSeCN to introduce the $SeCN^-$ vibrational probe, it was not clear if there was a very small long-term offset (0.012) in the anisotropy decay at the maximum delay time of 300 ps.[38] Here it was possible to take data to longer time, 500 ps, and it was found that the decay of the bulk liquid indeed goes to zero. Therefore, all of the data in the current study were fit without an offset. Fitting the bulk IL data without an offset slightly changed the anisotropy values obtained previously.[38] However, the differences in the bulk time constants from the earlier reported values do not influence the comparison to the data from the SILM samples as all of the data used in the current experiments were taken and fit in the same manner. The slowest time scale in the triexponential fits

DOI: 10.1021/jacs.6b10695
J. Am. Chem. Soc. 2017, 139, 311−323

Table 1. Parameters from the Triexponential Fits to the Anisotropy Decays

sample	A_1[a]	t_1 (ps)	A_2[a]	t_2 (ps)	A_3[a]	t_3 (ps)
bulk	0.08 ± 0.004	2.6 ± 0.3	0.14 ± 0.006	25.3 ± 2.2	0.13 ± 0.007	136.4 ± 5.5
PES200	0.10 ± 0.006	4.4 ± 0.5	0.16 ± 0.005	49.5 ± 4.3	0.08 ± 0.007	511.5 ± 74.9
PES30	0.09 ± 0.005	4.0 ± 0.4	0.14 ± 0.004	43.6 ± 3.0	0.11 ± 0.004	513.0 ± 35.0

[a] A_i is the amplitude of each exponential.

Table 2. Parameters from Wobbling Analysis

sample	θ_{in} (deg)[a]	θ_{c1} (deg)[b]	θ_{c2} (deg)[b]	θ_{tot} (deg)[c]	τ_{c1} (ps)[d]	τ_{c2} (ps)[d]	τ_m (ps)[d]	D_{c1} (10^{-3} ps^{-1})[e]	D_{c2} (10^{-3} ps^{-1})[e]
bulk	16.7 ± 1.8	24.0 ± 0.6	38.7 ± 0.9	47.3 ± 1.0	2.6 ± 0.3	31.1 ± 3.3	136 ± 6	19.0 ± 2.4	3.7 ± 0.5
PES200	18.5 ± 1.8	27.7 ± 0.8	47.0 ± 1.2	55.6 ± 1.2	4.4 ± 0.5	54.8 ± 5.3	512 ± 75	14.5 ± 2.0	2.8 ± 0.4
PES30	18.4 ± 1.3	25.4 ± 0.6	41.2 ± 0.6	50.3 ± 0.6	4.0 ± 0.4	47.6 ± 3.6	513 ± 35	13.6 ± 1.8	2.7 ± 0.3

[a] The inertial cone angle. [b] θ_{c1} and θ_{c2} are the first and second diffusive cone half angles. [c] The total cone half angle accounting for all three cones. [d] τ_{c1}, τ_{c2}, and τ_m are the decay times associated with the first and second diffusive cones and the final free diffusion, respectively. [e] D_{c1} and D_{c2} are the first and second cone diffusion constants.

to SILM data exceeds the experimental time window. The three time constants in a decay differ by a factor of approximately 10, e.g., ∼4 ps, ∼40 ps, and ∼500 ps. This separation of time scales makes it possible to obtain reasonably accurate values of the longest time constants in spite of the limited time range of the measurements. The uncertainty in the fits is reflected in the error bars, which are not overly large. Therefore, the values for the slowest time component of the SILM anisotropy data are of sufficient accuracy for comparison to the results on the bulk liquid.

From Figure 3 and Table 1 it is clear that confinement of the RTIL in the membrane pores slows the $SeCN^-$ orientational relaxation significantly compared to the bulk IL. In going from the bulk liquid to the SILMs, the first time constant slows from 2.6 ps to ∼4 ps. The second time constant slows from ∼25 ps to ∼45 ps, and the slowest decay time constant slows from ∼130 ps to ∼500 ps. The anisotropy decay constants for the PES200 and PES30 membranes are the same within experimental error. However, the amplitudes of the decays are not the same for the two membranes (see Table 1). The main feature is the increased amplitude of the slowest decay in the smaller pores of PES30 compared to PES200 with an associated decrease in amplitude for the faster components. So while the SILMs' time constants are the same within error, the data show that the dynamics in the small pores are slower because more reorientation occurs in the slowest component of the anisotropy decay.

As seen in eq 4, the anisotropy decay begins with a value of 0.4. However, the initial values of the anisotropy decays for both bulk and SILM samples are less than 0.4 when the experimental curves are extrapolated a short way back to $t = 0$ (see Figure 3). Ultrafast inertial orientational motion produces an initial drop in $r(t)$ that is obscured by the nonresonant signal that occurs around $t = 0$.[74] After the inertial drop, all of the data sets (points) are fit well with triexponential functions (solid curves) as discussed above. The multiexponential behavior of the anisotropy decay can be described in terms of the wobbling-in-a-cone model,[45−48,50,51] that is, a series of orientational relaxation processes, each of which is constrained to be in successively larger angular cones with complete diffusive orientational randomization occurring on the longest time scale.

In the wobbling-in-a-cone model, the orientational correlation function decays an amount determined by the cone angle. This level is expressed as the square of a generalized order parameter Q for a single cone

$$Q^2 = \left(\frac{1}{2}\cos\theta_0(1 + \cos\theta_0)\right)^2 \tag{5}$$

where θ_0 is the half angle of the cone.[45,46,48,49] Including wobbling motion in a single cone and complete orientational randomization yields the orientational correlation function as

$$C_2(t) = (Q^2 + (1 - Q^2)\exp(-t/\tau_c))\exp(-t/\tau_m) \tag{6}$$

where τ_c is the time constant for the restricted diffusion in the cone, and τ_m is the time constant for the final complete orientational randomization.[50] Since the anisotropy decays in the bulk and SILMs samples are triexponential and including the initial inertial drop, the orientational correlation function requires an inertial cone and two diffusive cones along with the final free diffusion. Therefore, the resulting form for $C_2(t)$ includes more order parameters and more time constants and is given by[51]

$$\begin{aligned} C_2(t) = {} & (1 - T^2)\exp(-t/\tau_{in}) + T^2(1 - S^2)\exp(-t/\tau_{c1}) \\ & + T^2S^2(1 - R^2)\exp(-t(1/\tau_{c2} + 1/\tau_m)) \\ & + T^2S^2R^2\exp(-t/\tau_m) \end{aligned} \tag{7}$$

where T, S, and R are the order parameters for the inertial and two diffusive cones, respectively. τ_{in} is the time constant for the inertial cone and is set to be much faster than our experimental time resolution. τ_{c1} and τ_{c2} are the time constants for the first and second diffusive cones, respectively. Using the resulting parameters from the triexponential fits (Table 1), eq 7 yields three cone angles for the inertial and two diffusive cones and three time constants for the two cones and the final diffusive complete randomization. Table 2 summarizes the resulting parameters from this "wobbling analysis". The cone angles represent the angular displacement for each class of restrictions, and the associated diffusion constants reflect the time constants for the relaxations.

The cone angles derived from the wobbling analysis show some differences among the samples (see Table 2). First, the bulk inertial cone angle is somewhat smaller than those from the SILMs, but the error bars overlap. In all of the samples the local IL structure surrounding $SeCN^-$ gives essentially the same available spaces for $SeCN^-$ to reorient through the ultrafast ballistic motion. The cone angles for the first and second cones increase in going form the bulk to the membranes. The increase in the PES200 membrane is larger than for PES30. For PES30, the increase over the bulk is small but outside of the error bars.

DOI: 10.1021/jacs.6b10695
J. Am. Chem. Soc. 2017, 139, 311−323

The total cone angle that is sampled prior to the complete orientational randomization is larger in the SILMs, with the increase less for PES30 than for PES200. However, the changes in the cone angles are small, indicating that there are only subtle differences in the local environment experienced by the $SeCN^-$ probe.

The associated decay times for the first and second cones, τ_{c1} and τ_{c2} in the SILMs are slower than in the bulk liquid, but with the decays faster in PES30 than in PES200. However, for comparing the wobbling dynamics, it is necessary to look at the orientational diffusion constant rather than the decay time because the diffusion constant depends on both the decay time and the cone angle.[42] The diffusion constants for the two cones, D_{c1} and D_{c2} are calculated from each cone angle and decay time.[46] For $\theta \leq 30°$,

$$D_c \cong 7\theta^2/24\tau_c \tag{8}$$

with θ in radians. For $\theta > 30°$, the full expression for any value of θ is used.[46]

$$D_c = \frac{x_c^2(1+x_c)^2\{\ln[(1+x_c)/2] + (1-x_c)/2\}}{\tau_c(1-Q^2)[2(x_c-1)]} + \frac{(1-x_c)(6+8x_c-x_c^2-12x_c^3-7x_c^4)}{24\tau_c(1-Q^2)} \tag{9}$$

where $x_c = \cos\theta$. From Table 2, it can be seen that both cone diffusion constants are smaller in the SILMs than in the bulk, and the diffusion constants in the SILMs are the same within error. Restrictions imposed by the local environmental structure predominantly govern the diffusive orientation in the two cones, rather than the bulk viscosity.[38] While both the first and second cone diffusion constants are somewhat smaller in the SILMs, the difference is not large. Thus, the similarity in the cone angles and diffusion constants of all of the samples indicates a substantial similarity in their local solvation environments.

However, the time to relax these local environments, as given by the τ_m, (see Table 2) is substantially longer in the SILMs then in the bulk liquid. In going from the bulk to the SILMs, the decay time constant for the free diffusion, τ_m, increases from 136 ps to ~512.0 ps. (The diffusion constant for this free diffusion is $D_m = 1/6\tau_m$.) This 3.8-fold increase is much larger than the changes in the cone diffusion constants. Previously, it was found that the complete orientational randomization of $SeCN^-$ is hydrodynamic in the bulk $EmimNTf_2$: the measured free diffusion time constants (88 ps) agreed well with the calculated values from Debye−Stokes−Einstein (DSE) theory under slip boundary conditions (74−126 ps).[38] In addition, τ_m increases proportionally with the viscosity of the bulk IL in going from $EmimNTf_2$ to $BmimNTf_2$.[38] This viscosity dependence demonstrates that the rearrangement of the RTIL structure is necessary for the relatively small anion, $SeCN^-$, to completely reorient in these ILs, and the IL rearrangement is the barrier that restricts the free orientational diffusion. (Note that τ_m for the bulk sample in this study (136.4 ps) is larger than previously reported value (88 ps) because the data were taken to longer time, which showed there was no offset in the anisotropy decay.) The significant increase of the free diffusion time constants in the SILMs shows that the IL rearrangement is significantly altered by the membrane.

The extent of the slowing of the IL rearrangement in the SILMs can be ascertained qualitatively by determining the "effective viscosity". We make the reasonable assumption that the shape and volume of the $SeCN^-$ is unchanged in going from bulk $EmimNTf_2$ to $EmimNTf_2$ in the SILMs. Then, τ_m is directly proportional to the viscosity according to the DSE equation. Using measured τ_m values for the bulk and SILMs samples and the bulk viscosity of $EmimNTf_2$ at room temperature (39.9 cP),[38,39] the effective viscosity for the SILMs is calculated to be 150.0 cP. This value is almost the same as the bulk viscosity of $DmimNTf_2$ (143.7 cP),[38,39] which has 10 carbons in the alkyl chain of the cation. The increase in effective viscosity over that of bulk $EmimNTf_2$ occurs in spite of the fact that the same IL is used in the SILM samples. The result indicates that there is a significant change in the time scale for the overall randomization of the IL structure in the SILMs, which suggests a change in the global IL structure.

3.4. 2D IR Measurements: Structural Dynamics. As discussed briefly in the Introduction, 2D IR spectroscopy can provide information about the structural evolution of a system by measuring the spectral diffusion of a vibrational probe molecule. Liquid structures that result in different intermolecular interactions with the probe are responsible for the inhomogeneous broadening of the vibrational absorption line. 2D IR spectroscopy measures spectral diffusion, which reports on how long it takes for the probe molecules to sample the frequencies in the inhomogeneously broadened line, and therefore, how long it takes to sample the liquid structures that give rise to inhomogeneous broadening. To quantify the amplitudes and time scales of the spectral diffusion, the results from the 2D IR experiments are analyzed in terms of the FFCF. The FFCF is the probability that a vibrational oscillator with an initial frequency in the inhomogeneous spectral distribution will have that same frequency at a later time, averaged over all initial frequencies.

Figure 4 displays 2D IR spectra of $SeCN^-$ in $EmimNTf_2$ confined in the pores of the PES200 SILM. The quality of the data is excellent in spite of the massive amount of scattered light generated by the membrane. At a short waiting time, T_w, when the liquid structure has had little time to evolve, the vibrational oscillator is likely to retain the same frequency as its initial frequency, and the 2D IR spectrum is diagonally elongated as shown in an upper panel of Figure 4 (T_w = 3 ps). The dashed line is the diagonal. At long time (bottom panel, T_w = 100 ps), the line shape has become more round because the vibrational oscillators' final frequencies (time of echo emission) have lost correlation with their initial frequencies because of structural evolution of the system.

The FFCF is modeled with a multiexponential form

$$C_{tot}(t) = \langle \delta\omega(t)\delta\omega(0)\rangle = \sum_i \Delta_i^2 \exp(-t/\tau_i) \tag{10}$$

where Δ_i and τ_i are the frequency fluctuation amplitudes and associated time constants, respectively, for the ith component. $\delta\omega(t) = \omega(t) - \langle\omega\rangle$ is the instantaneous frequency fluctuation and $\langle\omega\rangle$ is the average frequency. A component of the FFCF is motionally narrowed if $\Delta_i\tau_i \ll 1$, and its Δ and τ cannot be determined separately. The motionally narrowed contribution to the absorption spectrum (homogeneous broadening) has a pure dephasing line width given by $\Gamma^* = \Delta^2\tau/\pi = 1/\pi T_2^*$, where T_2^* is the pure dephasing time. However, the vibrational lifetime and orientational relaxation also contribute to the total homogeneous dephasing time, T_2 which is given by

DOI: 10.1021/jacs.6b10695
J. Am. Chem. Soc. 2017, 139, 311−323

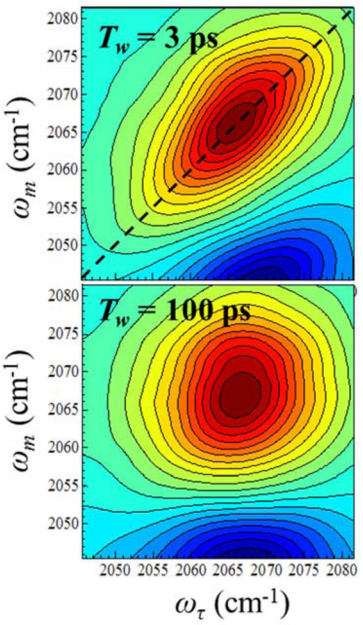

Figure 4. 2D IR spectra of the CN stretching mode of $SeCN^-$ in $EmimNTf_2$ ionic liquid in the nanopores of the SILM PES200. Top panel: the spectrum at short waiting time. The data show significant elongation along the diagonal, the dashed line. Bottom panel: the spectrum at longer time. The dynamical information, spectral diffusion, is obtained from the change in shape of the spectrum with T_w.

$$\frac{1}{T_2} = \frac{1}{T_2^*} + \frac{1}{2T_1} + \frac{1}{3T_{or}} \tag{11}$$

where T_1 and T_{or} are the vibrational lifetime and orientational relaxation time, respectively. Then, the total homogeneous line width is $\Gamma = 1/\pi T_2$. To extract the FFCF, we analyzed the line shape of the 2D IR spectrum as a function of T_w, using the CLS method.

Recent studies of polarization selective 2D IR experiments on various IL systems have shown that the probe molecules' orientational relaxation can contribute to spectral diffusion.[34,36−38] Orientational relaxation will contribute to spectral diffusion is if it occurs on similar time scales to the spectral diffusion caused by structural evolution of the sample, and if the sample produces an electric field at the vibrational probe that evolves slower or over a comparable time span than the reorientation.[34,36−38] In this regime, the reorientation of the $SeCN^-$ probe induces a change in its interaction with the electric field through the first order Stark effect and thus, the vibrational frequency changes. The contribution of RISD differs in two experimental polarization configurations, parallel ($\langle XXXX \rangle$) and perpendicular ($\langle XXYY \rangle$) as shown in the top panel of Figure 5.

The total spectral diffusion is the result of RISD and the structural spectral diffusion, SSD. We are interested in the structural spectral diffusion, which is caused by the structural evolution of the IL. For the first-order Stark effect coupling, the total FFCF is the product of the two contributions

$$C_{tot}^i(t) = F_{SSD}(t) R_i(t) \tag{12}$$

where $F_{SSD}(t)$ is the structural contribution from fluctuations in the liquid structure and $R_i(t)$ is the RISD contribution with

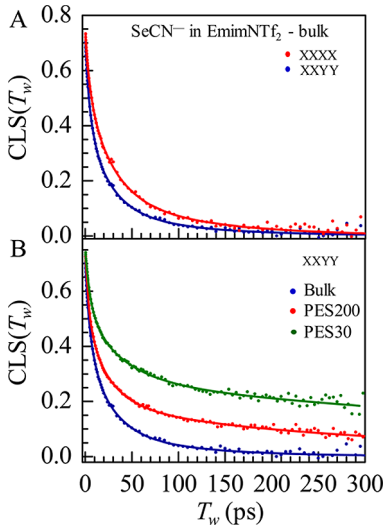

Figure 5. 2D IR CLS (normalized frequency-frequency correlation function) decay data (points) of (A) $SeCN^-$ in the bulk $EmimNTf_2$ from both the parallel and perpendicular polarization configurations and (B) bulk and SILM, PES200 and PES30, samples from the perpendicular polarization configuration. Each SILM decay curve is the average of measurements on three different samples. The solid lines are the fits to the data using the RISD theory to obtain the structural spectral diffusion.

i = parallel or perpendicular.[36,37] The RISD contribution is given by

$$R_{para}(t) = \frac{3}{25}\left[\frac{11C_1(t) + 4C_3(t)}{1 + 0.8C_2(t)}\right] \tag{13}$$

for the parallel configuration and

$$R_{perp}(t) = \frac{3}{25}\left[\frac{7C_1(t) - 2C_3(t)}{1 - 0.4C_2(t)}\right] \tag{14}$$

for the perpendicular configuration. In addition, the isotropic decay curve can be obtained by adding the parallel 2D spectrum to twice the perpendicular 2D spectrum (correctly normalized) at each T_w, and obtaining the CLS from these combined spectra. The isotropic RISD factor is given by

$$R_{iso}(t) = C_1(t) \tag{15}$$

The $C_1(t)$, $C_2(t)$, and $C_3(t)$ are the first, second, and third order Legendre polynomial orientational correlation functions, respectively.[36,37] $C_2(t)$ is obtained from the anisotropy measurements (see Figure 3). From $C_2(t)$, $C_1(t)$ and $C_3(t)$ are determined.[37] In using eq 12 to obtain the SSD, there are no adjustable parameters in the RISD term. The SSD can be obtained by fitting the SSD parameters to either the parallel or perpendicular CLS decay. Here we use the perpendicular decays (Figure 5B) because the perpendicular polarization configuration reduces the scattered light for the SILM samples. The SSD is modeled as a sum of exponentials.

Figure 5A displays the CLS decays (points) for the bulk sample and the parallel and perpendicular RISD/SSD fits (solid curves). The same SSD parameters were used for both CLS curves. Previously, SSD for $SeCN^-$ in the bulk sample was modeled as a biexponential with a small offset.[38] As mentioned above, better anisotropy data were obtained by experimental improvements that permitted the acquisition of data at longer times. The resulting changes in the anisotropy data resulted in

DOI: 10.1021/jacs.6b10695
J. Am. Chem. Soc. 2017, 139, 311−323

Table 3. Triexponential SSD Parameters from the RISD Fits

sample	A_1[a]	τ_1 (ps)	A_2[a]	τ_2 (ps)	A_3[a]	τ_3 (ps)
bulk	0.26 ± 0.08	6.0 ± 2.2	0.37 ± 0.08	32 ± 13	0.14 ± 0.10	140 ± 67
PES200	0.18 ± 0.04	3.9 ± 1.5	0.31 ± 0.04	24 ± 4	0.31 ± 0.01	504 ± 53
PES30	0.16 ± 0.05	7.3 ± 2.7	0.19 ± 0.04	40 ± 16	0.46 ± 0.02	1660 ± 630

[a] A_i is the amplitude of each exponential.

Table 4. Isotropic FFCF Parameters

sample	T_2 (ps)[a]	Γ (cm^{-1})[b]	Δ_1 (cm^{-1})[c]	τ_1 (ps)[d]	Δ_2 (cm^{-1})[c]	τ_2 (ps)[d]	Δ_3 (cm^{-1})[c]	τ_3 (ps)[d]
bulk	2.0	5.3	4.2 ± 0.4	3.8 ± 0.9	5.7 ± 0.3	20.6 ± 4.3	3.9 ± 0.5	82.3 ± 13.0
PES200	2.1	5.0	4.7 ± 0.3	3.9 ± 0.8	5.3 ± 0.2	25.8 ± 3.2	4.3 ± 0.1	341.4 ± 27.3
PES30	2.2	4.9	4.2 ± 0.3	5.4 ± 1.1	4.8 ± 0.2	37.9 ± 7.2	5.3 ± 0.2	756.2 ± 191.6

[a] T_2: homogeneous dephasing time. [b] Γ: homogeneous line width (fwhm). [c] Δ_i: inhomogeneous line width (standard deviation) of the ith component. [d] τ_i: decay time constant of the ith component.

improved quality in the SSD fitting with a triexponential functional form with no offset. Figure 5B shows the data for the bulk sample, PES200, and PES30 all with the perpendicular polarization configuration (points) and the fits (solid curves) in which only the SSD parameters are adjustable. As can be seen in Figure 5, in all cases the fits are very good. Table 3 summarizes the SSD time constants and their amplitudes from the fits. For the bulk sample, the first two time constants are similar to those previously reported from the RISD fits with the biexponential SSD. In addition, there is the slowest time constant of 140 ps with relatively smaller amplitude that was previously modeled as a constant offset.

As can be seen in Figure 5, the CLS decays for the SILM samples are significantly slower than the bulk sample. In addition, the decay for PES30 (smaller pores) is slower than the decay for PES200. The curves in Figure 5 have contributions from both SSD and RISD. Table 3 gives the SSD parameters after the contributions to the experimental decays from RISD have been removed. Table 4 (discussed further below) gives the decay time constants for the isotropic decay that is obtained directly from the experimental data, that is, it includes RISD, which makes the experimental decays faster than the SSD contribution to the FFCF. The slowest decay time is slower than the experimental window, but it can be extracted with reasonable accuracy for comparison to the bulk value because of the large separation in the slowest decay time constants from the faster decay time constants. The relatively large uncertainty is reflected in the error bars, which are still small enough to permit the comparison among the samples. The slowest SSD time constants (Table 3) are slower than the slowest FFCF time constants (Table 4) from which they are derived, and have correspondingly larger error bars. Again, the error bars are not too large to prevent comparison among the samples.

For the SSD parameters (Table 3), within experimental error, the fastest two time constants, τ_1 and τ_2, do not change in going from the bulk IL to the SILMs. However, it is noteworthy that the amplitudes, A_1 and A_2, decrease in going from the bulk IL to PES200 and decrease further going to PES30. So while the time constants may be the same or very similar, less of the structural dynamics occurs on the faster time scales. The shift in amplitude out of the faster components of the SSD explains why the curves shown in Figure 5B differ even at short time. However, the major change is in the slowest component of the SSD, τ_3. While the error bars are large, the trend falls far outside of the error. In going from the bulk sample to PES200, the structural evolution slows by ∼3.5, and then going from PES200 to PES30, the dynamics slow by another factor of ∼3. Thus, going from the bulk to the porous medium slows the IL dynamics and having smaller pores further slows the dynamics.

In a previous study of $SeCN^-$ dissolved in bulk RTILs (Emim, Bmim, Hmim, and Dmim NTf_2) it was observed that the short time component of the SSD, τ_1, is invariant to the chain length and bulk viscosity of the ILs.[39] It was proposed that the fast time scale insensitivity to the chain length is indicative of the ILs' small local motions that occur on a short time scale without major rearrangement of the global liquid structure. Here, τ_1 is also insensitive to the nature of the sample, bulk or membranes, indicating that small and fast local motions are not affected by confinement of the IL in the membrane pores even though there is a large increase in the effective viscosity. The invariance of τ_1 across the samples suggests that the local environment near the probe molecule is not fundamentally altered in the membranes, which is in line with the invariance of the FT-IR spectra and the vibrational lifetimes across samples. In addition to τ_1, τ_2 does not show a change in the dynamics in going from the bulk $EmimNTf_2$ to either membrane within experimental error. It is important to note that the time constants that describe the SSD arise from the multiexponential model used to fit the data. They should be considered time scales for a set of structural rearrangements rather than a time constant describing a single particular process. The results show that the time scales for structural rearrangements on the short and medium time range do not change in going from the bulk to confinement in the membranes. However, their contribution to the inhomogeneous broadening is reduced when the IL is confined in the membranes so that the amplitude of the slowest component, A_3 in Table 3, increases significantly in the progression bulk liquid, PES200, PES30. More of the structural rearrangement is occurring on the longest time scale in going from the bulk to increasingly smaller pores.

The slowest time constant of the SSD, τ_3, exhibits a substantial change in going from the bulk liquid to PES200 and then to PES30. While the error bars are large, there is a substantial slowing of the dynamics, well outside of error (see Table 3). Not only does τ_3 become longer, but as stated above, an increasing fraction of the dynamics occur on the longest time scale in going from bulk to large pores and, finally, to smaller pores. The long time scale dynamics reflected in τ_3 are probably associated with longer distance scales and more global rearrangements of the liquid structure. The FT-IR spectra (Figure 2) are essentially identical for the three liquids.

DOI: 10.1021/jacs.6b10695
J. Am. Chem. Soc. 2017, 139, 311−323

The homogeneous components of the absorption spectra are the same (see Table 4), which means the inhomogeneous broadening in the three samples is the same. Thus, confinement in the pores shifts the time evolution of some of the structures that give rise to the inhomogeneous broadening from shorter to longer times. In the bulk liquid, some of the structures that could rearrange rapidly are no longer able to do so in the pores. These results suggest that the global structure of the IL changes in the SILMs in a manner that affects the slowest and longest distance scale motions. This view is consistent with the discussion of the anisotropy decays (Section 3.3). The slowest component of the anisotropy decay, t_3, (see Table 1) becomes substantially longer in going from the bulk liquid to the IL confined in the pores. This component reflects the complete diffusive randomization of the probe orientation, and its slowdown implies an increased effective viscosity. However, within error, there is no difference in the slowest component of the anisotropy decay for the two pore sizes. The anisotropy decay is determined by how the evolution of the liquid structure influences the local structure in which the probe is reorienting. In contrast, SSD can be caused by distant liquid structural rearrangements through evolution of the electric field produced by the liquid at the site of the probe. Therefore, the anisotropy and the SSD observables, while both determined by the time evolution of the liquid structure, can be sensitive to different aspects of the evolution.

Figure 5B displays 2D IR data for the bulk liquid, PES200, and PES30 with perpendicular pulse polarizations ($\langle XXYY \rangle$). This data and the RISD expression of eq 14 were used to obtain the SSD parameters. In a molecular dynamics (MD) simulation, neither the perpendicular nor the parallel data are calculated because simulations of 2D IR data do not include polarized radiation fields that give rise to initial cosine-squared distribution of excited vibrations. MD simulations will contain the full dynamics, that is, SSD and RISD. Thus, MD simulations calculate the isotropic FFCF which contains the full dynamics, that is, SSD and RISD as $C_{tot}^{iso}(t) = F_{SSD}(t)R_{iso}(t)$ (eq 12) with $R_{iso}(t)$ given by eq 15. Using the SSD parameters obtained from the data, we calculated $C_{tot}^{iso}(t)$ for the SILM samples. From these and the FT-IR spectra, we obtained isotropic FFCF parameters, including the homogeneous line widths, which are given in Table 4. These parameters can be used for comparison to MD simulations.

3.5. Structures of EmimNTf$_2$ in the Membranes. The experimental results presented above show that the very local structure surrounding the $SeCN^-$ probe is little changed in the pores from that found in the bulk liquid. However, the IL dynamics experienced by the probe, particularly the slowest time scale dynamics that are likely related to longer nonlocal distance scales, are substantially influence by confinement of the IL in pores. In addition, the 2D IR experiments show that the effect of confinement in the pores is larger for the smaller pores of PES30 compared to PES200. The changes in dynamics with confinement are not caused by the presence of the vibrational probe at the wall of the pore. Because the pores are large, only a small fraction of the probes are at the wall, and interactions with a distinct molecular environment would cause changes in both the FT-IR spectrum and the vibrational lifetime, neither of which occurs. Therefore, the observed changes in dynamics must be caused by changes in the IL structural dynamics induced by the pore wall and felt throughout the liquid contained in the pores.

Because the pores are so large compared to the sizes of other types of systems in which nanoconfinement strongly influences liquid dynamics,[50,52−60] it initially seems surprising that bulk dynamics are not observed in the pores. However, there is substantial evidence that an interface can have a long distance scale influence on ILs. The structure of ILs near surfaces and in confined environments has been of interest for many years,[75−85] and there are ample review articles on this subject, highlighting intriguing aspects of IL structure at the interfaces.[86−91] Based on many experimental and computational studies, the most commonly accepted picture is that the interactions with interfaces can remarkably affect the structure of ILs, in particular, the ordering of cations and anions very near the interfaces, and this effect is local, limited within a few nanometer scale.

However, this restriction of the influence of an interface to the proximity of the interface has been challenged recently by several experimental studies that imply long-range ordering effects even over a micrometer length scale.[92−94] Using an extended surface forces apparatus, Espinosa-Marzal and co-workers demonstrated that the nanoconfinement imposed on a film of 1-hexyl-3-methylimidazolium ethylsulfate between mica surfaces can induce an ordered structure that extends over 60 nm from the surface.[93] Another study by Shaw and co-workers reported the transformation of IL films into a long-range ordered structure over 2 μm occurs when the NTf_2 anion-based IL films are formed by applying a slow shearing process.[94] In addition, a recent simulation study by Margulis and co-workers demonstrated that 1-methyl-3-octylimidazolium octylsulfate can form a lamellar structure at the vacuum interface, and it extends to the full length scale of their simulation (9 nm), explicating experimentally observed long-range ordering effects at the interfaces.[95]

The literature discussed above indicates a long distance scale influence on ILs by an interface. The results presented here, which show significant changes occur in dynamics in going from bulk EmimNTf$_2$ to EmimNTf$_2$ in the large pores of PES200 and PES30, provide substantial evidence that the polymer interface can have a long-range (~100 nm) influence on the IL. The fact that the slowdown in the dynamics is greater for the smaller pores in PES30 than in PES200 is consistent with the influence of the interface falling off over a distance of very approximately 100 nm.

4. CONCLUDING REMARKS

The structural dynamics of EmimNTf$_2$ in the bulk liquid were compared to those in the nanopores of two Supported Ionic Liquid Membranes, PES200 and PES30. PES200 has an average pore size of ~300 nm, while PES30 has and average pore size of ~100 nm. 2D IR and IR polarization selective pump−probe experiments were performed on the CN stretch of the vibrational probe, $SeCN^-$. In both SILMs, the absorption spectra and the vibrational lifetime of the CN stretch were unchanged from that of the bulk liquid. These results demonstrate that the immediate IL environments surrounding the vibrational probes in the SILMs are unchanged from those of the bulk liquid.

Anisotropy measurements (orientational relaxation) of the vibrational probe showed significant differences between the bulk IL and the IL in the pores of the SILMs. The orientational relaxation measurements fit to a triexponential decay in all three samples. The two shorter time components reflect restricted orientational relaxation, wobbling-in-a-cone, while the slowest decay component is the final complete diffusive orientational randomization. All three decay components showed substantial

DOI: 10.1021/jacs.6b10695
J. Am. Chem. Soc. 2017, 139, 311−323

slowing in going from the bulk IL to the IL in the membranes. The orientational relaxation decay time constants in the two membranes with different pores sizes are the same within error. In Figure 3, the decay in the PES30 is clearly slower than in PES200. This is caused by an increased amplitude of the slowest relaxation component rather than a change in the time constants. Thus, the smaller pores cause a shift of the orientational relaxation to longer time.

The 2D IR data, Figure 5B, show substantial slowing in going from the bulk IL to PES200, and further slowing for the PES30 membrane. The spectral diffusion data were separated into the reorientation induced spectral diffusion (RISD) component and the structural spectral diffusion (SSD) component. The SSD is related to the dynamics of the IL structure and is of interest here. The SSD was fit with a triexponential function. The two faster components of the decays are the same within experimental error for all three samples (Table 3). However, there is a significant shift in amplitude to the slowest component in going from the bulk IL to the IL in PES200 and a further shift in amplitude to the slowest component in going from PES200 to PES30. In addition, the slowest component of the SSD becomes substantially slower in going from bulk (140 ps) to PES200 (504 ps) to PES30 (1660 ps). The faster SSD components reflect the more local structural evolution of the IL. The slowest component depends on more global structural rearrangements. It is the slowest component of the SSD that undergoes the most dramatic changes.

The slowing of the IL dynamics in the pores of the SILMs is caused by confinement. However, the large pore sizes (PES200, ~300 nm; PES30, ~100 nm) show that the polymer interface has a long-range influence on the IL dynamics. In systems such as water in reverse micelles,[50,52−55] confinement slows water dynamics but only when the diameter is ~4 nm or less. The results presented here demonstrate that, in ILs, an interface can change the dynamics of the liquid far from the interface.

Room temperature ionic liquids are being studied for CO_2 capture applications, but in practice the RTIL is likely to be used in an SILM because of the many advantages. The results presented here show that the dynamical properties of bulk ILs, such as translational diffusion coefficients, may not be a good guide for the behavior of the same IL in a SILM. The current experiments were conducted on the vibrational probe $SeCN^-$ because of its long vibrational lifetime and the relative ease of preparing the sample compared to using gaseous CO_2 as the vibrational probe. Previous bulk RTIL studies[39,40] revealed that both $SeCN^-$ and CO_2 behave similarly in a series of RTILs. Both vibrational probes have the same functional forms of the anisotropy and 2D IR decays and display the same trends with increasing alkyl chain lengths. The $SeCN^-$ serves a reporter on the IL dynamics and how the dynamics and interactions change when the IL is confined in the SILM pores. While the values of the time constants are dependent on the particular vibrational probe, the nature of the changes from sample to sample will not depend on the probe. The results show that there is a major slowing of the IL dynamics when the IL is confined in the SILM. Experiments on CO_2 in SILMs are in progress. In addition to verifying the trends observed here, comparison of the results from two vibrational probes, $SeCN^-$ and CO_2, will provide additional information.

AUTHOR INFORMATION

Corresponding Author

*fayer@stanford.edu

ORCID

Michael D. Fayer: 0000-0002-0021-1815

Notes

The authors declare no competing financial interest.

ACKNOWLEDGMENTS

We thank Adam L. Sturlaugson for preparation of EmimSeCN. This work was funded by the Division of Chemical Sciences, Geosciences, and Biosciences, Office of Basic Energy Sciences of the U.S. Department of Energy through Grant # DE-FG03-84ER13251. Additional support came from the Stanford Center for Carbon Storage, which provided partial salary support for J.Y.S.

REFERENCES

(1) Dlugokencky, E.; Tans, P. NOAA/ESRL: 2016; http://www.esrl.noaa.gov/gmd/ccgg/trends/.

(2) Metz, B.; Davidson, O.; Coninck, H. d.; Loos, M.; Meyer, L. *IPCC Special Report on Carbon Dioxide Capture and Storage. Prepared by Working Group III of the Intergovernmental Panel on Climate Change*; Cambridge University Press: Cambridge, United Kingdom, 2005; p 442.

(3) Haszeldine, R. S. *Science* **2009**, *325*, 1647−1652.

(4) Anderson, S.; Newell, R. *Annu. Rev. Enviro. and Resour.* **2004**, *29*, 109−142.

(5) Boot-Handford, M. E.; Abanades, J. C.; Anthony, E. J.; Blunt, M. J.; Brandani, S.; Mac Dowell, N.; Fernandez, J. R.; Ferrari, M.-C.; Gross, R.; Hallett, J. P.; Haszeldine, R. S.; Heptonstall, P.; Lyngfelt, A.; Makuch, Z.; Mangano, E.; Porter, R. T. J.; Pourkashanian, M.; Rochelle, G. T.; Shah, N.; Yao, J. G.; Fennell, P. S. *Energy Environ. Sci.* **2014**, *7*, 130−189.

(6) Pires, J. C. M.; Martins, F. G.; Alvim-Ferraz, M. C. M.; Simões, M. *Chem. Eng. Res. Des.* **2011**, *89*, 1446−1460.

(7) Gibbins, J.; Chalmers, H. *Energy Policy* **2008**, *36*, 4317−4322.

(8) Szulczewski, M. L.; MacMinn, C. W.; Herzog, H. J.; Juanes, R. *Proc. Natl. Acad. Sci. U. S. A.* **2012**, *109*, 5185−5189.

(9) van Alphen, K.; van Voorst tot Voorst, Q.; Hekkert, M. P.; Smits, R. E. H. M. *Energy Policy* **2007**, *35*, 4368−4380.

(10) Viebahn, P.; Nitsch, J.; Fischedick, M.; Esken, A.; Schüwer, D.; Supersberger, N.; Zuberbühler, U.; Edenhofer, O. *Int. J. Greenhouse Gas Control* **2007**, *1*, 121−133.

(11) *Inventory of U.S. Greenhouse Gas Emissions and Sinks: 1990−2014*; U.S. EPA; http://www.epa.gov/ghgemissions/us-greenhouse-gas-inventory-report-1990-2014.

(12) Gislason, S. R.; Oelkers, E. H. *Science* **2014**, *344*, 373−374.

(13) Kintisch, E. *Science* **2016**, *352*, 1262−1263.

(14) Matter, J. M.; Stute, M.; Snæbjörnsdottir, S. Ó.; Oelkers, E. H.; Gislason, S. R.; Aradottir, E. S.; Sigfusson, B.; Gunnarsson, I.; Sigurdardottir, H.; Gunnlaugsson, E.; Axelsson, G.; Alfredsson, H. A.; Wolff-Boenisch, D.; Mesfin, K.; Taya, D. F. d. l. R.; Hall, J.; Dideriksen, K.; Broecker, W. S. *Science* **2016**, *352*, 1312−1314.

(15) Kenarsari, S. D.; Yang, D.; Jiang, G.; Zhang, S.; Wang, J.; Russell, A. G.; Wei, Q.; Fan, M. *RSC Adv.* **2013**, *3*, 22739−22773.

(16) Spigarelli, B. P.; Kawatra, S. K. *J. CO2 Util.* **2013**, *1*, 69−87.

(17) *Economic Assessment of Carbon Capture and Storage Technologies: 2011 Update*; Global CCS Institute, 2011; http://www.globalccsinstitute.com/publications/economic-assessment-carbon-capture-and-storage-technologies-2011-update.

(18) Bara, J. E.; Camper, D. E.; Gin, D. L.; Noble, R. D. *Acc. Chem. Res.* **2010**, *43*, 152−159.

(19) Ramdin, M.; de Loos, T. W.; Vlugt, T. J. *Ind. Eng. Chem. Res.* **2012**, *51*, 8149−8177.

(20) Zhang, X.; Zhang, X.; Dong, H.; Zhao, Z.; Zhang, S.; Huang, Y. *Energy Environ. Sci.* **2012**, *5*, 6668−6681.

(21) Brennecke, J. F.; Gurkan, B. E. *J. Phys. Chem. Lett.* **2010**, *1*, 3459−3464.

DOI: 10.1021/jacs.6b10695
J. Am. Chem. Soc. 2017, 139, 311−323

(22) Hasib-ur-Rahman, M.; Siaj, M.; Larachi, F. *Chem. Eng. Process.* **2010**, *49*, 313−322.
(23) Plechkova, N. V.; Seddon, K. R. *Chem. Soc. Rev.* **2008**, *37*, 123−150.
(24) Earle, M. J.; Esperanca, J. M. S. S.; Gilea, M. A.; Canongia Lopes, J. N.; Rebelo, L. P. N.; Magee, J. W.; Seddon, K. R.; Widegren, J. A. *Nature* **2006**, *439*, 831−834.
(25) Smiglak, M.; Reichert, W. M.; Holbrey, J. D.; Wilkes, J. S.; Sun, L.; Thrasher, J. S.; Kirichenko, K.; Singh, S.; Katritzky, A. R.; Rogers, R. D. *Chem. Commun.* **2006**, 2554−2556.
(26) Anderson, J. L.; Ding, R.; Ellern, A.; Armstrong, D. W. *J. Am. Chem. Soc.* **2005**, *127*, 593−604.
(27) Castner, E. W.; Margulis, C. J.; Maroncelli, M.; Wishart, J. F. *Annu. Rev. Phys. Chem.* **2011**, *62*, 85−105.
(28) MacDowell, N.; Florin, N.; Buchard, A.; Hallett, J.; Galindo, A.; Jackson, G.; Adjiman, C. S.; Williams, C. K.; Shah, N.; Fennell, P. *Energy Environ. Sci.* **2010**, *3*, 1645−1669.
(29) Scovazzo, P.; Visser, A. E.; Davis, J. H.; Rogers, R. D.; Koval, C. A.; DuBois, D. L.; Noble, R. D. Supported Ionic Liquid Membranes and Facilitated Ionic Liquid Membranes. In *Ionic Liquids*; American Chemical Society: Washington, D.C., 2002; Vol. *818*, pp 69−87.
(30) Lozano, L. J.; Godínez, C.; de los Ríos, A. P.; Hernández-Fernández, F. J.; Sánchez-Segado, S.; Alguacil, F. J. *J. Membr. Sci.* **2011**, *376*, 1−14.
(31) Dai, Z.; Noble, R. D.; Gin, D. L.; Zhang, X.; Deng, L. *J. Membr. Sci.* **2016**, *497*, 1−20.
(32) Tome, L. C.; Marrucho, I. M. *Chem. Soc. Rev.* **2016**, *45*, 2785−2824.
(33) Giammanco, C. H.; Kramer, P. L.; Yamada, S. A.; Nishida, J.; Tamimi, A.; Fayer, M. D. *J. Phys. Chem. B* **2016**, *120*, 549−556.
(34) Giammanco, C. H.; Kramer, P. L.; Yamada, S. A.; Nishida, J.; Tamimi, A.; Fayer, M. D. *J. Chem. Phys.* **2016**, *144*, 104506.
(35) Brinzer, T.; Berquist, E. J.; Ren, Z.; Dutta, S.; Johnson, C. A.; Krisher, C. S.; Lambrecht, D. S.; Garrett-Roe, S. *J. Chem. Phys.* **2015**, *142*, 212425.
(36) Kramer, P. L.; Nishida, J.; Giammanco, C. H.; Tamimi, A.; Fayer, M. D. *J. Chem. Phys.* **2015**, *142*, 184505.
(37) Kramer, P. L.; Nishida, J.; Fayer, M. D. *J. Chem. Phys.* **2015**, *143*, 124505.
(38) Tamimi, A.; Fayer, M. D. *J. Phys. Chem. B* **2016**, *120*, 5842−5854.
(39) Tamimi, A.; Bailey, H. E.; Fayer, M. D. *J. Phys. Chem. B* **2016**, *120*, 7488−7501.
(40) Giammanco, C. H.; Yamada, S. A.; Kramer, P. L.; Tamimi, A.; Fayer, M. D. *J. Phys. Chem. B* **2016**, *120*, 6698−6711.
(41) Cadena, C.; Anthony, J. L.; Shah, J. K.; Morrow, T. I.; Brennecke, J. F.; Maginn, E. J. *J. Am. Chem. Soc.* **2004**, *126*, 5300−5308.
(42) Torralba-Calleja, E.; Skinner, J.; Gutiérrez-Tauste, D. *J. Chem.* **2013**, *2013*, 16.
(43) Armand, M.; Endres, F.; MacFarlane, D. R.; Ohno, H.; Scrosati, B. *Nat. Mater.* **2009**, *8*, 621−629.
(44) Shirota, H.; Mandai, T.; Fukazawa, H.; Kato, T. *J. Chem. Eng. Data* **2011**, *56*, 2453−2459.
(45) Kinosita, K., Jr; Kawato, S.; Ikegami, A. *Biophys. J.* **1977**, *20*, 289−305.
(46) Lipari, G.; Szabo, A. *Biophys. J.* **1980**, *30*, 489−506.
(47) Wang, C.; Pecora, R. *J. Chem. Phys.* **1980**, *72*, 5333−5340.
(48) Kinosita, K., Jr; Ikegami, A.; Kawato, S. *Biophys. J.* **1982**, *37*, 461−464.
(49) Lipari, G.; Szabo, A. *J. Am. Chem. Soc.* **1982**, *104*, 4546−4559.
(50) Tan, H.-S.; Piletic, I. R.; Fayer, M. D. *J. Chem. Phys.* **2005**, *122*, 174501.
(51) Kramer, P. L.; Giammanco, C. H.; Fayer, M. D. *J. Chem. Phys.* **2015**, *142*, 212408.
(52) Tan, H.-S.; Piletic, I. R.; Riter, R. E.; Levinger, N. E.; Fayer, M. D. *Phys. Rev. Lett.* **2005**, *94*, 057405.
(53) Park, S.; Moilanen, D. E.; Fayer, M. D. *J. Phys. Chem. B* **2008**, *112*, 5279−5290.
(54) Fayer, M. D.; Levinger, N. E. *Annu. Rev. Anal. Chem.* **2010**, *3*, 89−107.
(55) Fayer, M. D. *Physiology* **2011**, *26*, 381−392.
(56) Anastasiadis, S.; Karatasos, K.; Vlachos, G.; Manias, E.; Giannelis, E. *Phys. Rev. Lett.* **2000**, *84*, 915−918.
(57) Loughnane, B. J.; Farrer, R. A.; Scodinu, A.; Reilly, T.; Fourkas, J. T. *J. Phys. Chem. B* **2000**, *104*, 5421−5429.
(58) Richert, R. *Annu. Rev. Phys. Chem.* **2011**, *62*, 65−84.
(59) Thompson, W. H. *Annu. Rev. Phys. Chem.* **2011**, *62*, 599−619.
(60) Krutyeva, M.; Wischnewski, A.; Monkenbusch, M.; Willner, L.; Maiz, J.; Mijangos, C.; Arbe, A.; Colmenero, J.; Radulescu, A.; Holderer, O. *Phys. Rev. Lett.* **2013**, *110*, 108303.
(61) Wang, P.; Zakeeruddin, S. M.; Moser, J.-E.; Humphry-Baker, R.; Grätzel, M. *J. Am. Chem. Soc.* **2004**, *126*, 7164−7165.
(62) Barrett, E. P.; Joyner, L. G.; Halenda, P. P. *J. Am. Chem. Soc.* **1951**, *73*, 373−380.
(63) Ramakrishnan, S.; McDonald, C.; Prud'homme, R.; Carbeck, J. *J. Membr. Sci.* **2004**, *231*, 57−70.
(64) Kumar, S. K.; Tamimi, A.; Fayer, M. *J. Chem. Phys.* **2012**, *137*, 184201.
(65) Tokmakoff, A. *J. Chem. Phys.* **1996**, *105*, 1−12.
(66) Kwak, K.; Park, S.; Finkelstein, I. J.; Fayer, M. D. *J. Chem. Phys.* **2007**, *127*, 124503.
(67) Kwak, K.; Rosenfeld, D. E.; Fayer, M. D. *J. Chem. Phys.* **2008**, *128*, 204505.
(68) ASTM, *F316−03(2011), Standard Test Methods for Pore Size Characteristics of Membrane Filters by Bubble Point and Mean Flow Pore Test*; ASTM International: West Conshohocken, PA, 2011.
(69) Yun, S. J.; Lim, J. W.; Lee, J.-H. *Electrochem. Solid-State Lett.* **2004**, *7*, C13−C15.
(70) Yuan, R.; Yan, C.; Tamimi, A.; Fayer, M. D. *J. Phys. Chem. B* **2015**, *119*, 13407−13415.
(71) Schmidt, J.; Corcelli, S.; Skinner, J. *J. Chem. Phys.* **2005**, *123*, 044513.
(72) Kenkre, V.; Tokmakoff, A.; Fayer, M. *J. Chem. Phys.* **1994**, *101*, 10618−10629.
(73) Owrutsky, J.; Raftery, D.; Hochstrasser, R. *Annu. Rev. Phys. Chem.* **1994**, *45*, 519−555.
(74) Moilanen, D. E.; Fenn, E. E.; Lin, Y.-S.; Skinner, J.; Bagchi, B.; Fayer, M. D. *Proc. Natl. Acad. Sci. U. S. A.* **2008**, *105*, 5295−5300.
(75) Antelmi, D. A.; Kékicheff, P.; Richetti, P. *Langmuir* **1999**, *15*, 7774−7788.
(76) Atkin, R.; Warr, G. G. *J. Phys. Chem. C* **2007**, *111*, 5162−5168.
(77) Mezger, M.; Schröder, H.; Reichert, H.; Schramm, S.; Okasinski, J. S.; Schöder, S.; Honkimäki, V.; Deutsch, M.; Ocko, B. M.; Ralston, J. *Science* **2008**, *322*, 424−428.
(78) Sieffert, N.; Wipff, G. *J. Phys. Chem. C* **2008**, *112*, 19590−19603.
(79) Bovio, S.; Podesta, A.; Lenardi, C.; Milani, P. *J. Phys. Chem. B* **2009**, *113*, 6600−6603.
(80) Mezger, M.; Schramm, S.; Schröder, H.; Reichert, H.; Deutsch, M.; De Souza, E. J.; Okasinski, J. S.; Ocko, B. M.; Honkimäki, V.; Dosch, H. *J. Chem. Phys.* **2009**, *131*, 094701.
(81) Coasne, B.; Viau, L.; Vioux, A. *J. Phys. Chem. Lett.* **2011**, *2*, 1150−1154.
(82) Hayes, R.; Borisenko, N.; Tam, M. K.; Howlett, P. C.; Endres, F.; Atkin, R. *J. Phys. Chem. C* **2011**, *115*, 6855−6863.
(83) Shimizu, K.; Pensado, A.; Malfreyt, P.; Pádua, A. A.; Lopes, J. N. C. *Faraday Discuss.* **2012**, *154*, 155−169.
(84) Mezger, M.; Ocko, B. M.; Reichert, H.; Deutsch, M. *Proc. Natl. Acad. Sci. U. S. A.* **2013**, *110*, 3733−3737.
(85) Elbourne, A.; Voïtchovsky, K.; Warr, G. G.; Atkin, R. *Chem. Sci.* **2015**, *6*, 527−536.
(86) Lynden-Bell, R. M.; Del Pópolo, M. G.; Youngs, T. G.; Kohanoff, J.; Hanke, C. G.; Harper, J. B.; Pinilla, C. C. *Acc. Chem. Res.* **2007**, *40*, 1138−1145.
(87) Santos, C. S.; Baldelli, S. *Chem. Soc. Rev.* **2010**, *39*, 2136−2145.
(88) Merlet, C.; Rotenberg, B.; Madden, P. A.; Salanne, M. *Phys. Chem. Chem. Phys.* **2013**, *15*, 15781−15792.

DOI: 10.1021/jacs.6b10695
J. Am. Chem. Soc. 2017, 139, 311−323

(89) Greaves, T. L.; Drummond, C. J. *Chem. Rev.* **2015**, *115*, 11379−11448.
(90) Hayes, R.; Warr, G. G.; Atkin, R. *Chem. Rev.* **2015**, *115*, 6357−6426.
(91) Rotenberg, B.; Salanne, M. *J. Phys. Chem. Lett.* **2015**, *6*, 4978−4985.
(92) Parr, D.; Chrestenson, J.; Malik, K.; Molter, M.; Zibart, C.; Egan, B.; Haverhals, L. M. *ECS Trans.* **2015**, *66*, 35−42.
(93) Jurado, L. A.; Kim, H.; Arcifa, A.; Rossi, A.; Leal, C.; Spencer, N. D.; Espinosa-Marzal, R. M. *Phys. Chem. Chem. Phys.* **2015**, *17*, 13613−13624.
(94) Anaredy, R. S.; Shaw, S. K. *Langmuir* **2016**, *32*, 5147−5154.
(95) Amith, W. D.; Hettige, J. J.; Castner, E. W.; Margulis, C. J. *J. Phys. Chem. Lett.* **2016**, *7*, 3785−3790.

DOI: 10.1021/jacs.6b10695
J. Am. Chem. Soc. 2017, 139, 311−323